J Mater Sci (2019) 54:1275–1290

Composites

Facile fabrication of BiOCl/RGO/protonated g-C_3N_4 ternary nanocomposite as Z-scheme photocatalyst for tetracycline degradation and benzyl alcohol oxidation

Jinjuan Xue[1], Xinyao Li[1], Shuaishuai Ma[2], Peng Xu[2], Mingxin Wang[1,*], and Zhaolian Ye[2,*]

[1] School of environmental and Safety Engineering, Changzhou University, Changzhou 213164, People's Republic of China
[2] College of Chemistry and Environmental Engineering, Jiangsu University of Technology, Changzhou 213001, People's Republic of China

Received: 7 June 2018
Accepted: 30 August 2018
Published online: 5 September 2018

ABSTRACT

A novel ternary BiOCl/RGO/PCN nanocomposite was successfully fabricated through coupling-protonated g-C_3N_4 (PCN) sheets with GO by electrostatic attraction, followed by in situ synthesis of BiOCl layers on the surface on PCN/GO via hydrothermal reaction and simultaneously achieving the reduction in GO. The as-prepared BiOCl/RGO/PCN composite exhibited significantly enhanced photoactivities toward the degradation of representative antibiotic tetracycline and selective aerobic oxidation of benzyl alcohol compared to pristine g-C_3N_4, protonated g-C_3N_4, pure BiOCl and binary BiOCl/PCN composite under simulated solar light irradiation. The structure–property relationship was explored by several effective characterization techniques. The results show that RGO coordinated well with two semiconductors of BiOCl and PCN, and BiOCl/RGO/PCN composite with closely contacted interface exhibited broad optical adsorption range and effective photogenerated charge carrier separation efficiency, which are attributed to the improved photocatalytic performance. The results also demonstrate that a Z-scheme charge process was formed between BiOCl and PCN with RGO serving as electron transfer medium to promote the fast transporting of photoinduced electrons. Therefore, more photoinduced electrons and holes could retain in the CB of PCN and in the VB of BiOCl with strong redox ability, respectively, which is beneficial to the further effective generation of active radicals participating in photocatalytic reaction. This work provides a promising Z-scheme ternary photocatalyst with facile synthetic method and potential application in environmental pollution elimination and green oxidative organic transformation.

Address correspondence to E-mail: wmx@cczu.edu.cn; bess_ye@jsut.edu.cn

https://doi.org/10.1007/s10853-018-2880-5

Introduction

Semiconductor photocatalysis, which not only can decompose environmental pollutants and produce hydrogen from water splitting but also can drive green organic synthesis, is an effective way to deal with the worldwide environmental purification and energy-shortage problems [1–3]. Among a variety of photocatalysts, the Z-scheme photocatalysts could simulate the natural photosynthesis process with high photocatalytic performance under visible-light illumination, becoming a research hot spot in recent years [4–6]. In a Z-scheme photocatalytic system, the photoinduced electrons would transfer from the more positive CB in a semiconductor to the more negative VB in another coupled semiconductor, obtaining the maximum overpotentials as well as the efficient separation of photogenerated charge pairs [7, 8].

Recently, a metal-free semiconductor g-C_3N_4 has become a promising catalyst in the field of photocatalysis due to its easy preparation, physical and chemical stability, appropriate band gap and fascinating electronic property [9–11]. However, as a single semiconductor, the photocatalytic activity of g-C_3N_4 is still limited by the narrow responsive range of visible light and the fast recombination of photoinduced carriers. As reported, constructing g-C_3N_4-based heterojunctions with matched band structures is an effective way to address the aforementioned problems [12–15]. In particular, g-C_3N_4-based Z-scheme heterojunctions have sparked more research attention due to the special transfer way of photoinduced electrons. To date, several g-C_3N_4-based Z-scheme heterojunctions have been developed, such as g-C_3N_4/Ag_3PO_4 [16, 17], g-C_3N_4/TiO_2 [18], g-C_3N_4/BiOI [19], and g-C_3N_4/MoS_2 [20]. The Z-scheme heterojunctions exhibited the obvious dual enhancements on the spatial separation of charge carriers and the strong redox ability in the photocatalytic reactions.

BiOCl is a layered semiconductor with wide band gap of 3.5 eV and has been used as an excellent UV-light-driven photocatalyst [21]. Since the band structure positions of g-C_3N_4 (E_{CB}= –1.12 eV, E_{VB}= + 1.57 eV) and BiOCl (E_{CB}= + 0.10 eV, E_{VB}= + 3.5 eV) matched well [22], BiOCl is an ideal heterojunction partner with g-C_3N_4 to form Z-scheme photocatalytic system. Furthermore, as we know, when an electron mediator is introduced in the Z-scheme heterojunction, more effective electron transfer would be achieved. Normally, noble metals and carbon nanomaterials with good electroconductivity have been applied as the electron mediators in Z-scheme photocatalytic system, such as g-C_3N_4/Au/BiOBr [23], g-C_3N_4/Ag/Ag_3VO_4 [24], g-C_3N_4/CNTs/Bi_2MoO_6 [25], and NGQD-modified g-C_3N_4/Bi_2WO_6 [26] heterojunctions. However, the exploration of g-C_3N_4-based Z-scheme photocatalysts with higher surface area, more active reaction sites, fast separation of photoinduced charge pairs and extended photoresponse range is still underway.

Over the past few years, antibiotic residues have been frequently detected in water environment along with the extensive use of antibiotics in human therapy and the farming industry [27]. Antibiotic residues in aqueous system have the potential to induce negative environmental effects even in low concentrations, including antibiotic resistance to bacteria, perturbations in ecosystems and possible risks to human health through drinking water and food-chain [28]. Tetracycline (TC) represents a major proportion of the antibiotics currently in use and, it is quite persistent in water and soil [29], resulting in potential harmfulness on living ecosystems. It is essential to develop appropriate methods for typical antibiotic TC removal. Nowadays, semiconductor photocatalysis appears to be a green technique for TC removal compared to the conventional adsorption and microbial degradation methods. Recent publications demonstrate that TC can be effectively degraded by g-C_3N_4-based photocatalysts, such as CDs/g-C_3N_4/MoO_3 Z-scheme photocatalyst [30], g-C_3N_4/Bi_3TaO_7 nanocomposite photocatalyst [31], and CoO/g-C_3N_4 p–n heterojunction photocatalyst [32]. Recently, organic transformations over photocatalysts by using solar energy also have attracted increasing attention since the synthesis process is environment friendly and relatively low cost [33, 34]. In particular, photocatalytic oxidation of alcohols to ketones or aldehydes is of great significance for bringing functionality into petroleum-based feedstocks [35]. Till now, photocatalytic oxidation of benzyl alcohol to benzaldehyde has been successively developed over photocatalysts such as Au–Pd/LDH [36], sulfuric acid-modified g-C_3N_4 [37], and VO@g-C_3N_4 [38]. The continuous exploration of effective photocatalysts for both pollutants degradation and green oxidative organic transformations is still on the way. Fe(III)-modified BiOBr was fabricated for improved photocatalytic benzyl alcohol oxidation and dye pollutants degradation [39], Ramacharyulu

reported MgO/g-C_3N_4 photocatalyst for 4-nitrophenol degradation and benzyl alcohol oxidation [40]. The photocatalysts for both antibiotic TC degradation and benzyl alcohol oxidation are rarely reported. In our previous work, we have developed 3D marigold-like Bi_2WO_6/Ag_2O/CQDs heterostructure with visible-light-driven photocatalytic activity toward tetracycline degradation and benzyl alcohol oxidation [41].

Based on the background and consideration mentioned above, in this work, we report a ternary heterojunction consisting of BiOCl layers and protonated g-C_3N_4 (PCN) sheets, with reduced graphene oxide (RGO) attaching on the surfaces of the two semiconductors as an electron transfer mediator. PCN/GO binary composite was first formed by electrostatic attraction, following that BiOCl combined with PCN/GO by a simple in situ synthesis method, and then, BiOCl/RGO/PCN was obtained through hydrothermal process. The as-prepared BiOCl/RGO/PCN ternary composite exhibited remarkably improved photocatalytic activities in the degradation of representative antibiotic TC and selective oxidation of benzyl alcohol in comparison with the corresponding binary composite or bare semiconductors under simulated solar light irradiation. Such designed ternary photocatalyst can show effective charge transfer as well as broadened photoresponsive range with the introduction of RGO. Furthermore, a probable photocatalysis mechanism over BiOCl/RGO/PCN photocatalyst was proposed in view of the radical trapping experiments and results demonstrated that the Z-scheme mechanism is more reasonable than the traditional double charge transfer mechanism in BiOCl/RGO/PCN photocatalyst.

Experimental

Preparation of photocatalysts

Pristine g-C_3N_4 (CN) was synthesized by polymerization of melamine at 550 °C with a heating rate of 2 °C/min under air atmosphere for 4 h. Graphite oxide (GO) colloid (solid content ~ 2.13 wt%) was prepared by the modified Hummers' method as reported previously [42]. PCN was prepared by the protonation of g-C_3N_4. Typically, 0.5 g of g-C_3N_4 was dispersed in 100 mL of HCl (2 mol/L) solution under ultrasound for 60 min, and the suspension was further stirred for 6 h. Then, the light yellow powder was collected after centrifugation and washed until the pH close to neutral. For the synthesis of BiOCl/RGO/PCN sample, 0.3521 g of GO colloid was first dispersed in 65 mL of ethylene glycol solution by ultrasonic treatment. Then, 0.15 g of PCN powder was added to the above suspension (the mass ratio of PCN to GO is 20:1) and ultrasonicated for another 60 min. After that, 0.2793 g $Bi(NO_3)_3{\cdot}5H_2O$ and 0.0336 g NaCl were dissolved into the above suspension and stirred vigorously for 30 min, then the solution was transferred into a Teflon-lined stainless-steel autoclave (100 mL) and heated at 140 °C for 8 h. The obtained product was collected by centrifugation, washed, and vacuum-dried at 60 °C overnight. The mass ratio of BiOCl, PCN and GO was calculated to be 20:20:1 in BiOCl/RGO/PCN sample. At the same time, BiOCl/PCN sample was also synthesized by the same method without the addition of GO. An additional hydrothermal reaction with GO as the only reaction precursor was also performed, and the hydrothermal reaction conditions including the solvent (ethylene glycol) is as same as that of the synthesis of BiOCl/RGO/PCN sample. After reaction, the obtained product was collected by centrifugation, washed, and vacuum-dried at 60 °C overnight.

Characterization

The structure and crystallinity of the as-prepared catalysts were analyzed by powder X-ray diffraction (XRD) on a D/max 2000 PC diffractometer (Rigaku), employing Cu Kα radiation (λ = 0.15401 Å) operated at 40 kV at a scan rate of 0.02° s^{-1} in the 2θ range from 10° to 80°. Fourier transform infrared (FTIR) spectra were performed on a Nicolet 370 FTIR spectrometer (Thermo Nicolet, USA) using pressed KBr pellets in the region of 500–4000 cm^{-1}. The morphology and microstructure of the samples were investigated by field emission scanning electron microscopy (FE-SEM, SUPRA55 SAPPHIRE, Zeiss) at an acceleration voltage of 5 kV and transmission electron microscopy (TEM, JEM-2100, JEOL) operating at 120 kV. X-ray photoelectron spectroscopy (XPS) was performed on a PerkinElmer PHI 5300 XPS spectrometer with Mg Kα (1253.6 eV) radiation as the excitation source to investigate the chemical states of the elements. UV–Vis diffuse reflectance spectra (DRS) were obtained by an UV–vis spectrophotometer (UV-2700, Shimadzu) using $BaSO_4$ as a reflectance

standard, and the data were recorded in the range of 300–800 nm. The N_2 adsorption–desorption isotherms were measured on a surface aperture adsorption instrument (ASAP 2020, Micromeritics USA) by N_2 physisorption at 77 K. Electrochemical impedance spectroscopy (EIS) measurements were carried out on a CHI920 workstation. Photoluminescence (PL) spectra were detected with a Horiba Jobin–Yvon fluorescence spectrophotometer at an excitation wavelength of 365 nm.

Photocatalytic activity tests

The photocatalytic experiments were carried out in a photochemical reactor equipped with reflux water to keep the temperature constant. And a 500-W xenon lamp (emitting wavelengths over the range 300–1000 nm) was used as the simulated solar light source. (1) *Photocatalytic degradation of tetracycline* (*TC*). In a typical photocatalytic degradation test, 20 mg of the photocatalyst was dispersed in TC aqueous solution (10 mg L^{-1}, 40 mL) and the suspension was magnetically stirred in the dark for 60 min to achieve adsorption–desorption equilibrium before light illumination. During the degradation reaction, 1 mL of the suspension was withdrawn at preselected time intervals and filtered through a 0.45-μm PTFE syringe filter to remove the particles. The concentration of TC in the liquid was analyzed by a high-performance liquid chromatography (HPLC, Shimadzu LC-20A). (2) *Photocatalytic oxidation of benzyl alcohol*. In a typical photocatalytic oxidation test, 50 mg of the photocatalyst was dispersed in 10 mL acetonitrile with the addition of 0.5 mmol benzyl alcohol. Prior to irradiation, the quartz reactor was saturated with O_2 and the suspension was stirred for 60 min in the dark. After irradiation for 10 h with O_2 bubbling, the reaction solution was centrifuged to remove the particles and the products in clear liquid were determined by a gas chromatography (GC, Agilent GC-7820A). The conversion and selectivity were defined as the following calculation formulas [43]:

$$\text{Conversion}(\%) = \frac{(C_0 - C_t)}{C_0} \times 100$$

$$\text{Selectivity}\ (\%) = \frac{C_p}{(C_0 - C_t)} \times 100$$

where C_0 is the initial concentration of the benzyl alcohol, C_p and C_t are the concentrations of the benzyl alcohol and benzaldehyde when the reaction time is t, respectively.

Results and discussion

Catalysts characterization

The crystalline nature and structure of the as-prepared catalysts were studied by XRD (Fig. 1). In Fig. 1a, two typical diffraction peaks at 13.1° and 27.5° assigned to (001) and (002) crystal planes can be observed, corresponding to the in-plane structure of tri-s-triazine units and interlayer stacking of the conjugated aromatic groups, respectively [44]. It is noted that the peak positions for PCN are the same as that of CN, indicating that the acidification process has no influence on crystalline phase of CN. As for pure BiOCl sample, all the diffraction peaks well corresponded to the tetragonal phase of BiOCl (JCPDS No. 06-0249) [45]. For BiOCl/PCN and BiOCl/RGO/PCN sample, both of the characteristic peaks of PCN and BiOCl appeared in the XRD patterns aside from 13.1°, which may be resulted from the overlap of other strong peaks. However, no obvious diffraction peak for RGO can be found in BiOCl/RGO/PCN sample, which is resulted from the low RGO content and weak intensity of RGO [46]. In order to verify whether GO can be transformed into RGO after hydrothermal reaction, we performed an additional hydrothermal reaction with GO as the only reaction precursor. Figure 1b shows the XRD patterns of precursor GO and the product after hydrothermal reaction with GO as the only reaction precursor. The main characteristic peak at 2θ = 23.5° corresponding to the (002) plane of RGO [47] can be found in the XRD pattern of sample 2, while the precursor GO (sample 1) shows an intensive characteristic (001) peak at 2θ = 11.4°, indicating that GO was transformed into RGO after hydrothermal reaction.

The morphology and microstructure of the as-prepared samples were investigated by FE-SEM and TEM. As can be seen from Fig. 2a, the clear stacking edge demonstrated that pristine CN owns two-dimensional lamellar structure, while PCN exhibited a smaller thin sheet-shaped morphology with diameters of 100–200 nm (Fig. 2b), implying that the acid treatment caused pristine CN break into small sheets with decreased size. Figure 2c shows that the pure

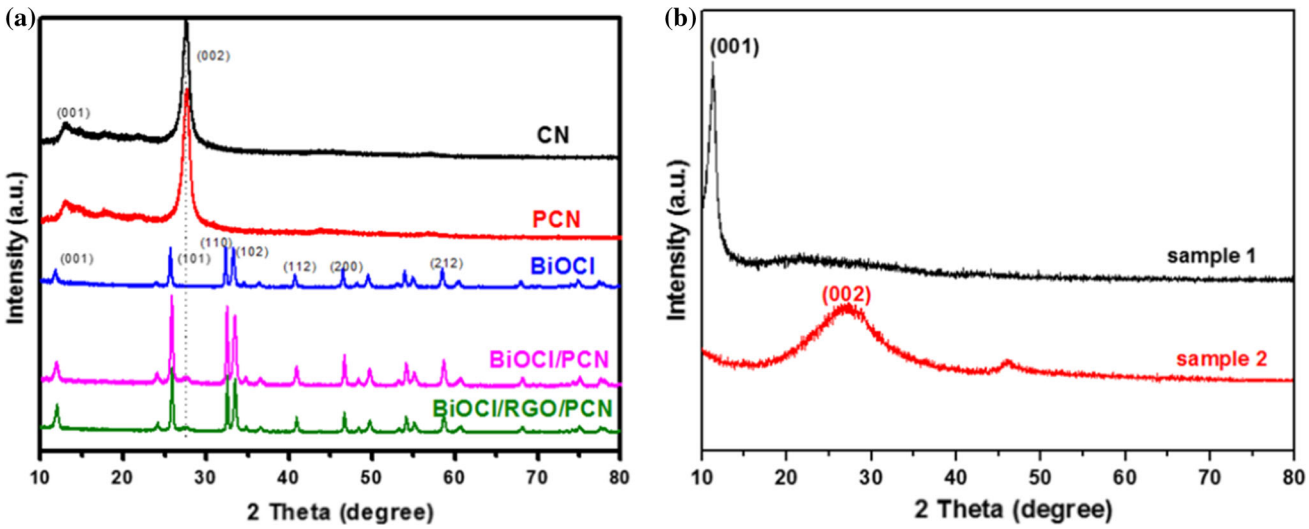

Figure 1 **a** XRD patterns of CN, PCN, BiOCl, BiOCl/PCN and BiOCl/RGO/PCN samples, **b** XRD patterns of precursor GO (sample 1) and the product after hydrothermal reaction with GO as the only reaction precursor (sample 2).

BiOCl has a nanoplate morphology and the nanoplates tend to form a spherical superstructure. The detailed morphology of BiOCl can be further observed from TEM images. Figure 3a clearly shows that the size of BiOCl nanoplates is 100–200 nm with thickness of about 20 nm. Interestingly, the TEM image of BiOCl (Fig. 3b) at high resolution displays that the nanoplate is made up of plenty of BiOCl nanocrystals with the size of 8–10 nm. Typical morphologies of BiOCl/RGO/PCN composite are illustrated well in Figs. 2d and 3c, from which PCN and BiOCl are wrapped well and infiltrated with RGO, demonstrating that the three components coordinated well in the heterojunction. The HRTEM image (Fig. 3d) exhibits two different lattice intervals of 0.344 nm and 0.275 nm, which can be assigned to (101) plane and (110) plane of BiOCl, respectively [48, 49].

Figure 4a shows the FTIR spectra of as-prepared CN, PCN, BiOCl and BiOCl/RGO/PCN samples. As for pristine CN, the peaks in 1200–1700 cm^{-1} region, including the peaks at 1638, 1569, 1410, 1320 and 1241 cm^{-1}, can be assigned to the typical stretching modes of CN heterocycles in g-C_3N_4 [26]. And the peak located at 807 cm^{-1} is attributed to the characteristic breathing vibration mode of the tri-s-triazine units in g-C_3N_4 framework [50]. In addition, the broad peak at around 3000–3500 cm^{-1} is attributable to O–H stretching vibrations of surface-absorption water molecules [51]. The FTIR spectrum of PCN shows the same feature curve as that of pristine CN, implying that protonation process did not change the phase structure of g-C_3N_4. As can be seen, the FTIR spectrum of BiOCl shows a peak at 524 cm^{-1}, which is attributed to the Bi–O stretching mode [52, 53]. Furthermore, the BiOCl/RGO/PCN sample shows a combined spectra of BiOCl and g-C_3N_4. However, the characteristic absorption peak of COO^- from the surface functional groups of RGO (site about 1460 cm^{-1}) was hard to be distinguished due to the low RGO content in BiOCl/RGO/PCN sample and the overlap of the strong band in the 1200–1700 cm^{-1} region for g-C_3N_4.

UV–Vis diffuse reflectance spectra were recorded to reveal the optical properties of the as-prepared samples. As illustrated in Fig. 4b, the adsorption spectrum of CN exhibits a steep edge at about 450 nm, which can be assigned to the band gap transition, whereas that of PCN exhibited a redshift to the wavelength of 460 nm. According to the formula of the band gap value of the semiconductor: $\lambda = 1240/E_g$ (λ is the limiting wavelength, E_g is the band gap energy), the band gap energies for CN and PCN were determined to be about 2.75 and 2.69 eV, respectively, implying that the protonation treatment endows g-C_3N_4 to process narrower band gap. For pure BiOCl, the adsorption edge is located around 375 nm and has no adsorption in the visible-light region. When coupling BiOCl with PCN, the BiOCl/PCN sample shows optical response to visible light. Moreover, it is noted that an obvious enhancement on optical absorption intensity in wavelengths

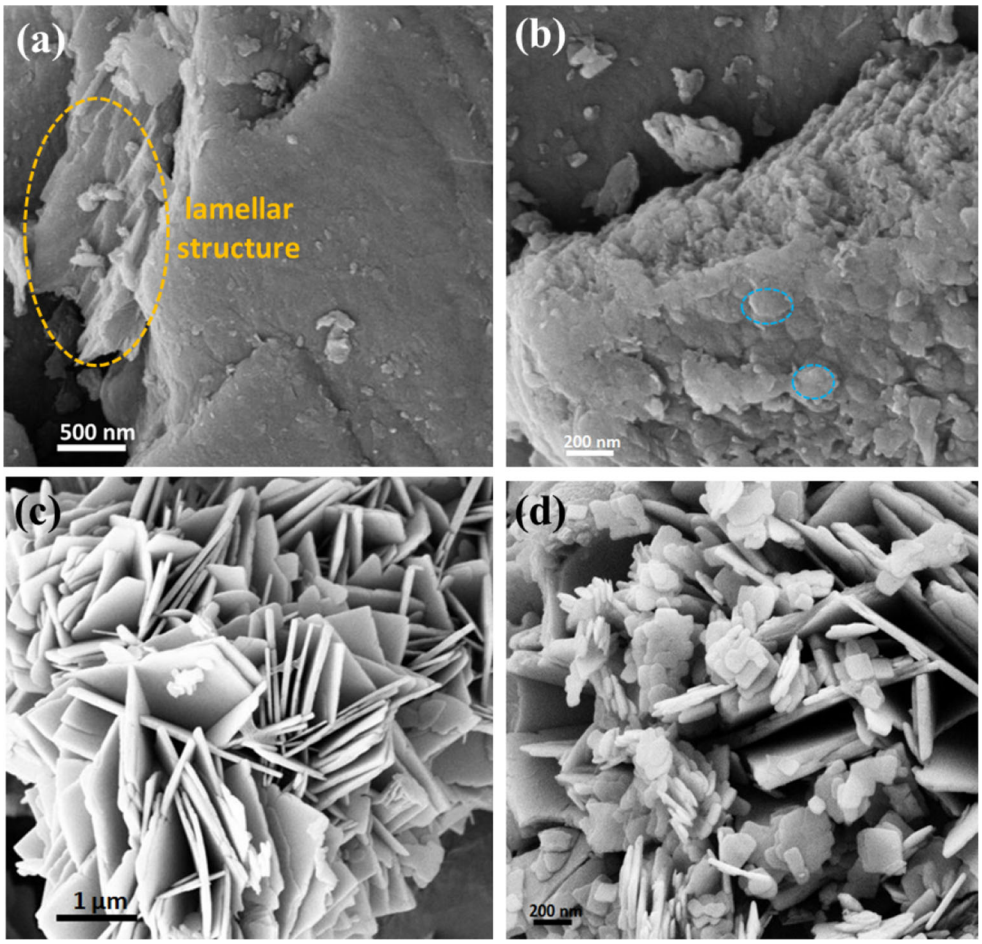

Figure 2 FESEM images of pristine CN (**a**), PCN (**b**), pure BiOCl (**c**), and BiOCl/RGO/PCN composite (**d**).

ranging from 350 to 800 nm can be achieved with the introduction of RGO in BiOCl/RGO/PCN sample. The above results demonstrate that BiOCl/RGO/PCN can take advantage of more solar energy, leading to the generation of more photogenerated charge carriers under visible-light irradiation.

The surface area and pore structure of BiOCl/RGO/PCN sample were analyzed by N_2 adsorption–desorption isotherms and pore size distribution curve (Fig. 4c, d). As can be seen, BiOCl/RGO/PCN, BiOCl/PCN and PCN samples exhibit a type-IV isotherm and a type-H3 hysteresis loop, implying the presence of slit-shaped pores aggregated from flake-like materials [50, 54, 55]. The pore size distribution curve for BiOCl/RGO/PCN sample also certifies that mesopores are presented in the composite. Parameters obtained from N_2 adsorption–desorption experiments are listed in Table 1. The specific surface area values are 6.399, 37.931, 57.068, 64.422 m^2/g for CN, PCN, BiOCl/PCN and BiOCl/RGO/PCN samples, respectively. It is found that CN turned into smaller sheets in morphology after protonation process and the specific surface area of PCN (37.931 m^2/g) is nearly six times higher than that of CN. Thus, the photocatalytic activity of PCN is expected to be improved compared to CN. Moreover, the combination of BiOCl with PCN further increased the specific surface area and the introduction of a small amount of GO into the composite resulted in a small increase in specific surface area. As expected, BiOCl/RGO/PCN photocatalyst would exhibit enhanced adsorption ability to the reaction substrates, which further contributes to the improved photocatalytic activity.

The XPS spectra were carried out to further reveal the detailed elemental composition and chemical status of BiOCl/RGO/PCN sample. Figure 5a shows the survey XPS spectrum of BiOCl/RGO/PCN composite, in which the binding energies of Bi 4f, Cl 2p, C 1s, N 1s, O 1s appeared at the corresponding photoelectron peaks, respectively. From Fig. 5b, two

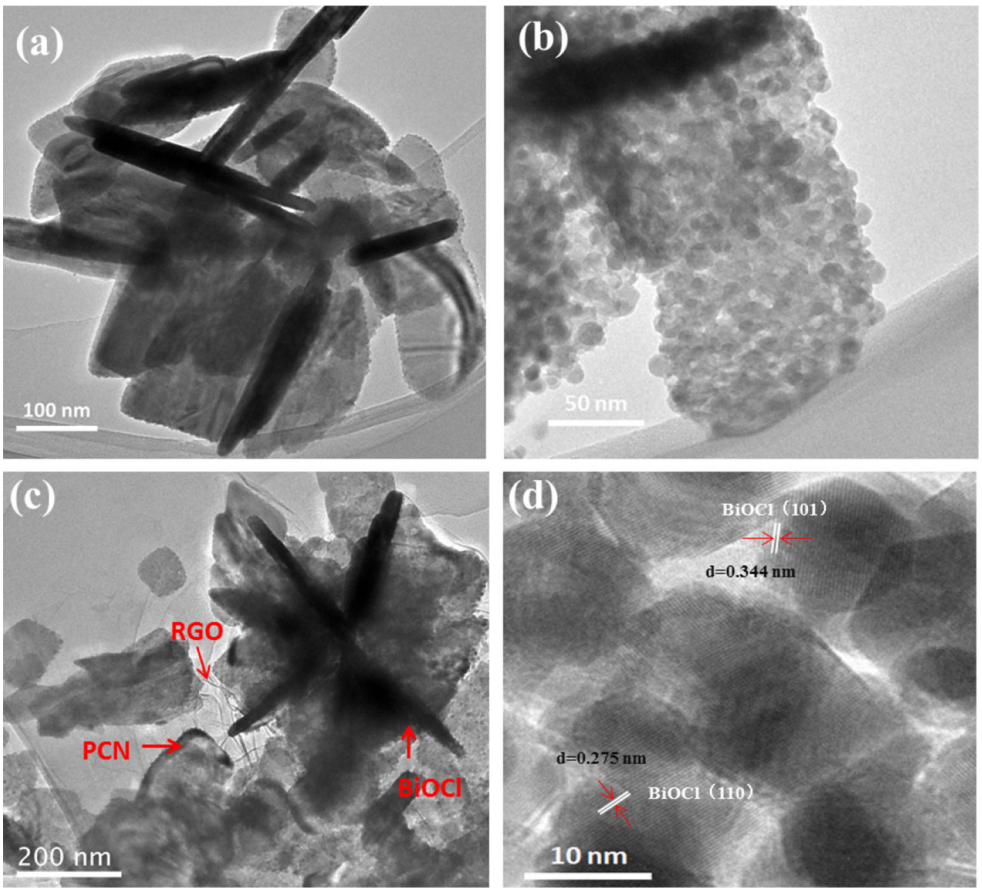

Figure 3 TEM images of pure BiOCl (**a**, **b**), BiOCl/RGO/PCN composite (**c**) and HRTEM image of BiOCl/RGO/PCN (**d**).

binding energy peaks at 159.5 and 164.9 eV can be observed, which are assigned to Bi $4f_{7/2}$ and Bi $4f_{5/2}$, respectively [48]. The N 1s spectrum (Fig. 5c) consists of three fitted peaks at 399, 399.7 and 401.2 eV, corresponding to sp^2-hybridized C=N–C bond, N–$(C)_3$ coordination, and N–H bond in the framework of graphitic-like carbon nitride, respectively [56, 57]. Besides, XPS spectrum of C 1s in Fig. 5d can be deconvoluted into three peaks at 284.7, 285.5 and 288.7 eV, which are related to sp^2 C–C bonds in graphitic carbon, C=N–C and N=C–N_2 bonds in graphitic-like carbon nitride, respectively [28]. It is noted that no peak for C–O bond from graphene oxide can be found in C 1s spectrum, indicating that GO has been reduced to RGO in hydrothermal reaction with alcohol solution as the solvent.

Photoluminescence characterization is performed in order to investigate the separation efficiency of photoinduced electron–hole pairs. It is known that a weaker PL intensity is an indication of a lower recombination of electron–hole pairs [58]. As shown in Fig. 6a, the PL spectra of CN, PCN, BiOCl/PCN and BiOCl/RGO/PCN samples all display strong emission peaks at around 460 nm, which are consistent with the emission characteristic of g-C_3N_4. It is found that PCN exhibited a weaker PL intensity than that of pristine CN, suggesting lower recombination of charge carriers in protonated g-C_3N_4. Significantly, the PL intensity is quenched after BiOCl coupling, and even becomes much lower for BiOCl/RGO/PCN composite. The experimental outcome reveals that the separation of photogenerated electrons and holes in composites is more efficient than pure PCN. In particular, BiOCl/RGO/PCN composite exhibits the highest charge-separation efficiency among the as-prepared samples and is expected to have the best photocatalytic activity.

Figure 6b depicts the electrochemical impedance spectroscopy (EIS) Nyquist plots of CN, PCN, BiOCl/PCN and BiOCl/RGO/PCN samples, which is adopted to evaluate the migration and transfer abilities of photoexcited charge carriers. Apparently, BiOCl/PCN and BiOCl/RGO/PCN composites exhibited smaller diameter of the inconspicuous arcs

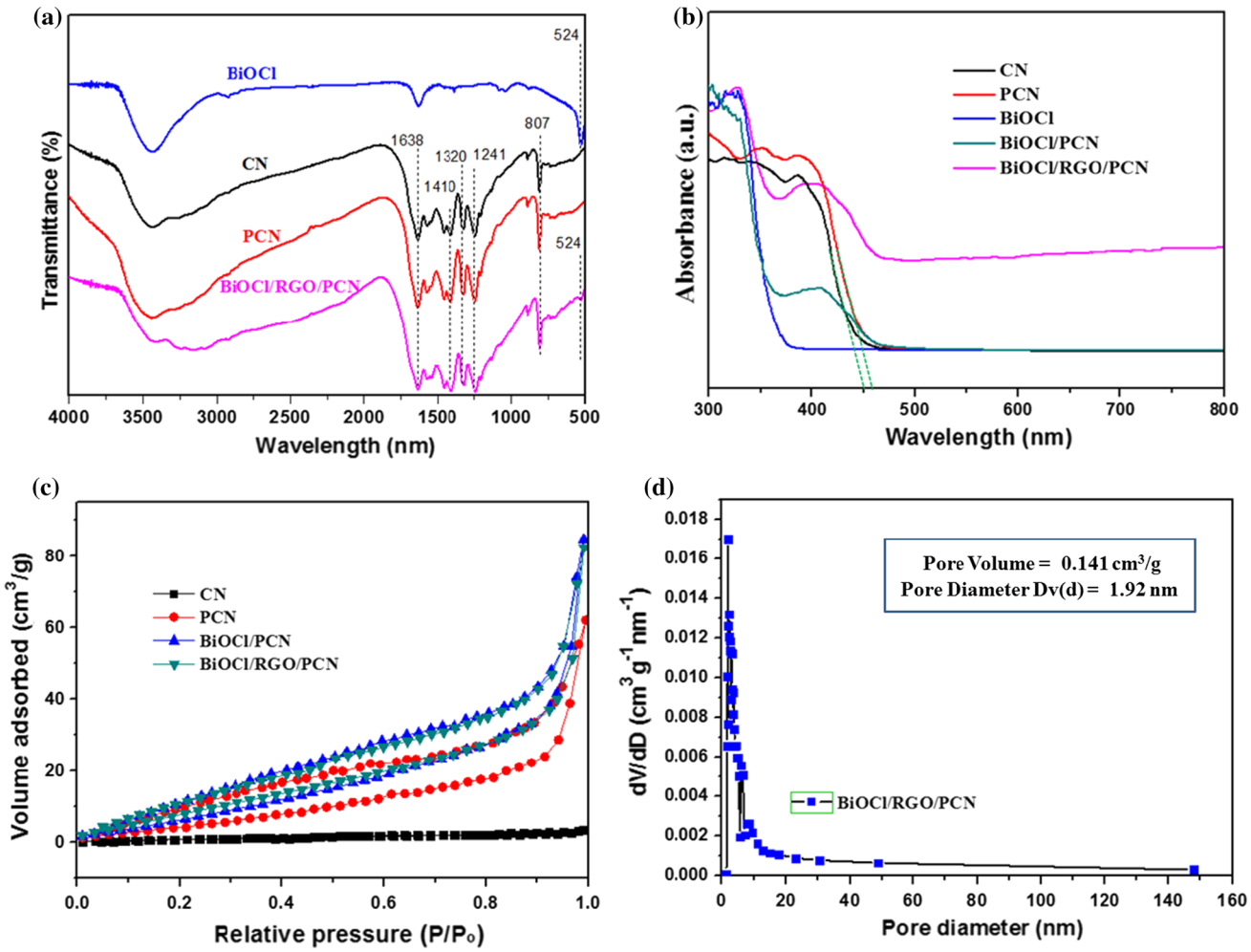

Figure 4 **a** FTIR spectra of CN, PCN, BiOCl and BiOCl/RGO/PCN samples, **b** UV–vis diffuse reflectance spectra of CN, PCN, BiOCl and BiOCl/RGO/PCN samples, **c** N_2 adsorption–desorption isotherms of CN, PCN, BiOCl/PCN and BiOCl/RGO/PCN samples, **d** pore size distribution curve of BiOCl/RGO/PCN composite.

Table 1 Parameters obtained from N_2 adsorption–desorption experiments

Sample	S_{BET} (m^2/g)	V_{pore} (cm^3/g)	D_{pore} (nm)
CN	6.399	0.007	3.611
PCN	37.931	0.105	2.185
BiOCl/PCN	57.068	0.144	3.057
BiOCl/RGO/PCN	64.422	0.141	1.920

in the high-frequency region compared to pristine CN and pure PCN, implying the lower electronic resistance of the composites [51]. The smallest arc radius on the EIS Nyquist plot of BiOCl/RGO/PCN sample can be observed, indicating that the electron mobility enhanced and an efficient separation of photogenerated electron–hole pairs has been achieved [59], which is consistent with the PL characterization conclusion.

Photocatalytic degradation performances

The photocatalytic performances of all synthesized catalysts were evaluated by photodegradation of TC under simulated solar light illumination, and the results are displayed in Fig. 7a. The curve shows that for the adsorption step in the dark, BiOCl/RGO/PCN composite exhibited the highest adsorption of around 23.6% among all of the samples. The introduction of RGO and the porous structure piled up by PCN and BiOCl within the composite probably contributed to such good adsorption ability. As depicted, pristine CN showed relatively low TC degradation rate of 23.3% within 180 min of irradiation, while the

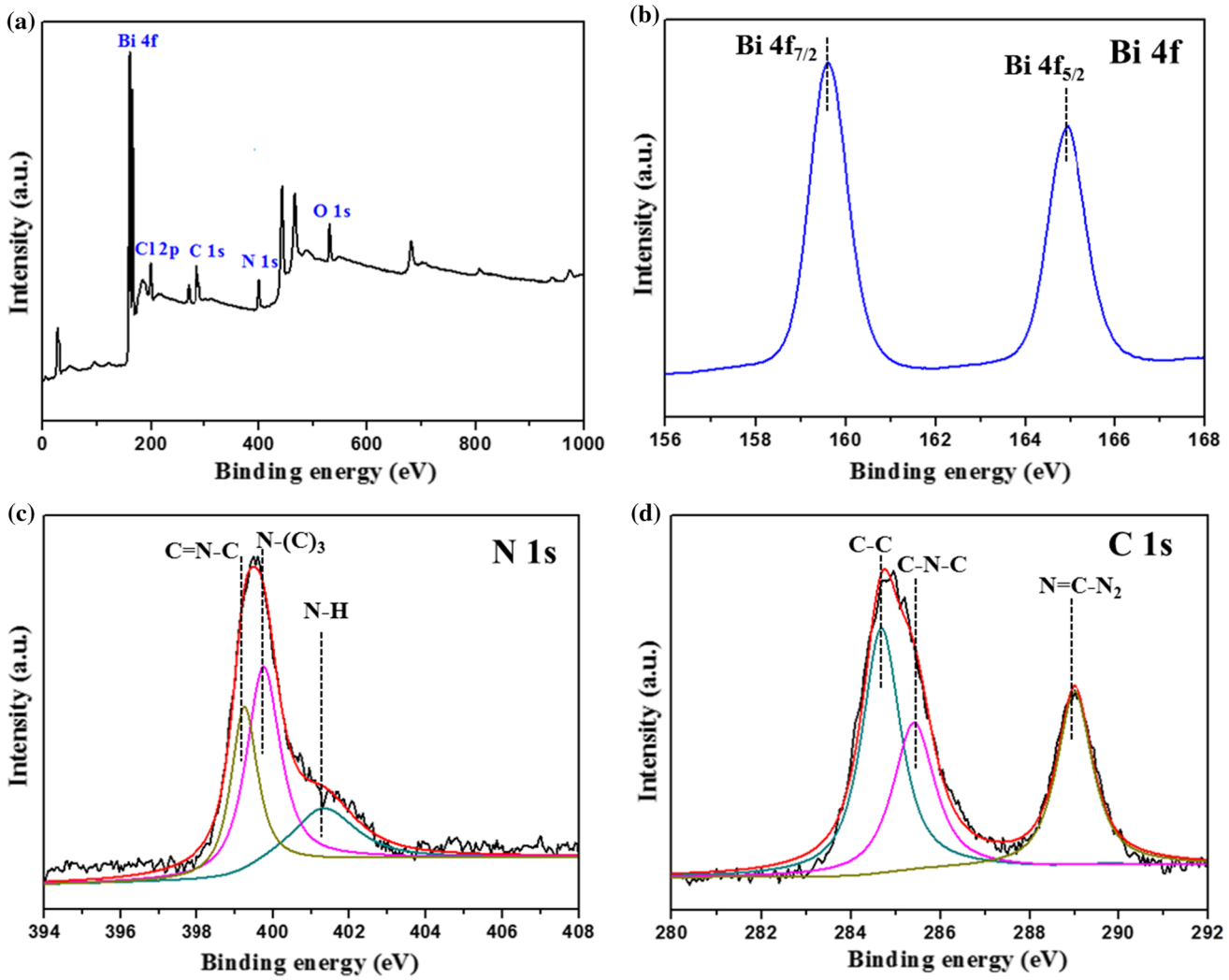

Figure 5 **a** The survey XPS spectrum and the corresponding high-resolution XPS spectra of **b** Bi 4f, **c** N 1s, **d** C1s of BiOCl/RGO/PCN composite.

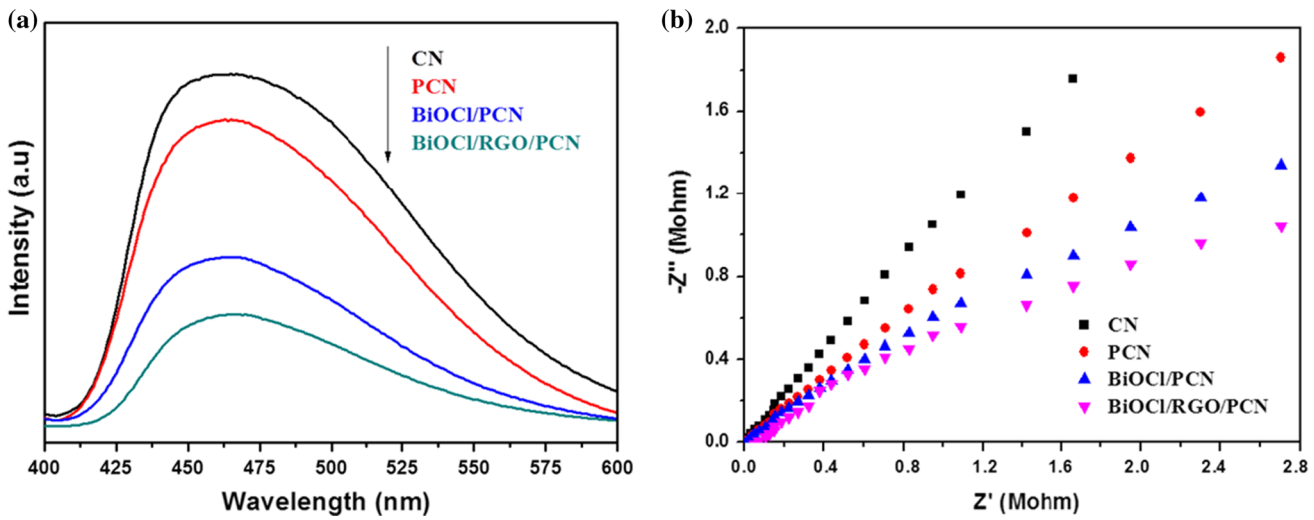

Figure 6 **a** Photoluminescence spectra and **b** EIS Nyquist plots of CN, PCN, BiOCl/PCN and BiOCl/RGO/PCN samples.

protonation of g-C_3N_4 can promote the photocatalytic activity to some extent, in which 42.9% TC degradation rate was obtained for PCN sample. After the same irradiation time, TC degraded around 40.3% over pure BiOCl catalyst. Compared to pure PCN and BiOCl, the coupling of PCN and BiOCl obviously improved the photodegradation efficiency. As expected, BiOCl/RGO/PCN sample displayed the best degradation efficiency, leading to almost 96.1% photodegradation of TC after the same irradiation time. As shown in Fig. 7b, the photocatalytic reaction rate can be described by the pseudo-first-order kinetic equation: $-\ln(C/C_0) = kt$, where k is the kinetic rate constant. It can be figured out form Fig. 7b that corresponding kinetic constants (k) over CN, PCN, BiOCl, BiOCl/PCN and BiOCl/RGO/PCN photocatalysts are 0.001, 0.002, 0.003, 0.008 and 0.0158 min^{-1}, respectively. Significantly, BiOCl/RGO/PCN presents the highest rate constant, which is 15.8 times higher than that of pristine CN. The enhanced activity of BiOCl/RGO/PCN can be ascribed to the formation Z-scheme heterojunction for effective separation of photoinduced charge carriers, and the incorporation of RGO in the composite also helped to extend the optical response range as well as achieve more effective electron transfer.

Catalyst stability evaluation and radical trapping experiments

Recyclability experiment was carried out to ascertain the utility of the catalyst for practical applications. Five successive runs were performed over BiOCl/RGO/PCN photocatalyst (Fig. 8a). It can be found that the photodegradation rate of TC reduced to 84.3% after five cycles, where exhibiting slight decline rather than obvious decrease compared to the first run. The result suggests the adequate stability and the reusability of BiOCl/RGO/PCN in organic pollutants elimination. In addition, a series of radical trapping experiments were performed in order to understand the primary reactive species involved in the degradation reaction over BiOCl/RGO/PCN photocatalyst under visible-light irradiation. Here, *t*-BuOH, *p*-benzoquinone and EDTA were introduced to scavenge $^{\cdot}OH$, $^{\cdot}O_2^-$ and h^+, respectively. As shown in Fig. 8b, the photodegradation rate of TC was about 96.1% without scavengers in the reaction after irradiation for 180 min. It is noted that the addition of *p*-benzoquinone (1 mM) obviously decreases the photodegradation rate for the same irradiation time, implying that $^{\cdot}O_2^-$ plays an important role in the reaction. A similar inhibition phenomenon is occurred with the introduction of EDTA (1 mM), demonstrating that h^+ is also an important reactive species. However, when *t*-BuOH (1 mM) was added into reaction solution, it almost unchanged for the degradation rate, manifesting that $^{\cdot}OH$ barely involved in the reaction. According to the above results, we can deduce that $^{\cdot}O_2^-$ and h^+ are the main reactive species for TC photodegradation in the reaction system over BiOCl/RGO/PCN photocatalyst.

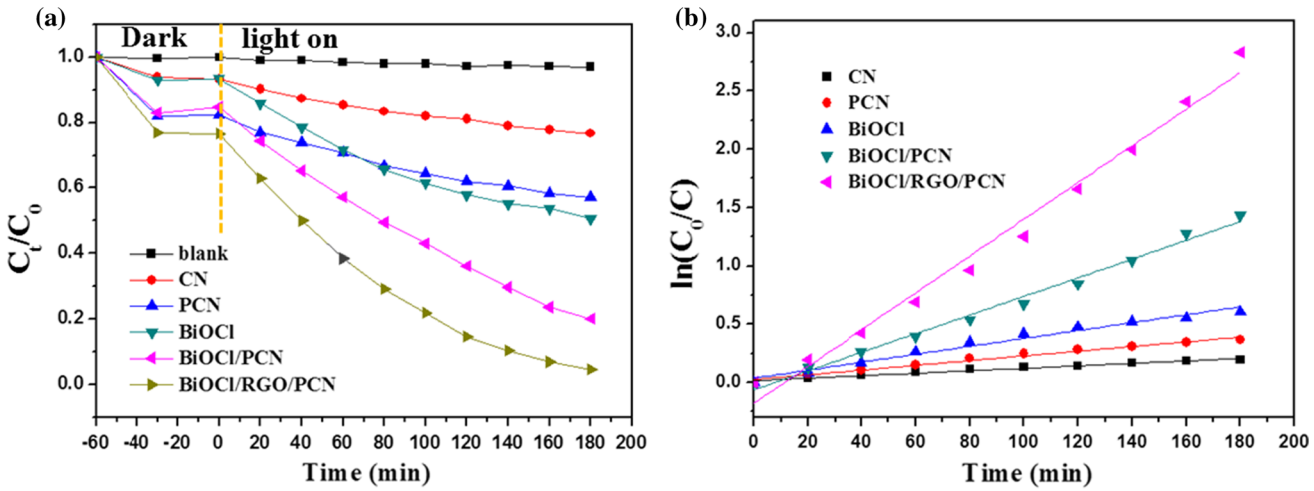

Figure 7 **a** Photocatalytic activities and **b** kinetics of the as-prepared samples for TC degradation under simulated solar light irradiation.

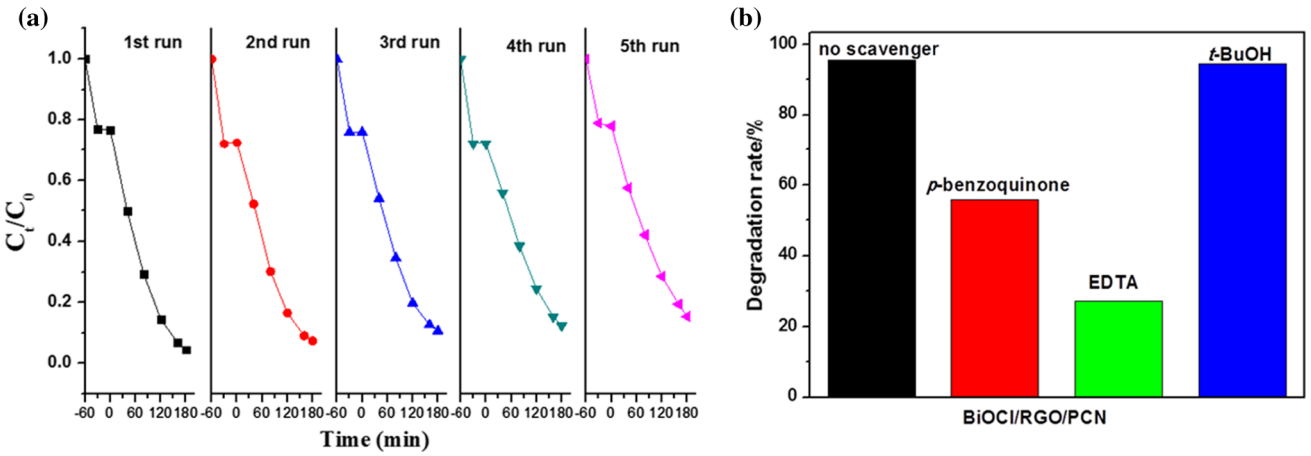

Figure 8 **a** Five photocatalytic degradation cycles of TC, **b** TC degradation rates in the presence of different radical scavengers over BiOCl/RGO/PCN after xenon lamp irradiation for 180 min.

Photocatalytic oxidation activities

Recent reports demonstrated that g-C_3N_4-based catalysts have exhibited appreciable results for the selective oxidation of benzyl alcohol to benzaldehyde with O_2 as the benign oxidant [60–62], and the key for raising the product selectivity is to avoid the generation of nonselective species $^{\cdot}OH$ radicals during photocatalysis process [63]. Since the above radical trapping results confirmed that $^{\cdot}OH$ species barely involved in the photocatalytic system over BiOCl/RGO/PCN catalyst, we infer that BiOCl/RGO/PCN composite is a potential visible-light-driven photocatalyst for selective oxidation of benzyl alcohol. Table 2 shows the photocatalytic performance of the selective aerobic oxidation of benzyl alcohol to benzaldehyde by the as-prepared catalysts. Up to 10 h visible-light illumination, BiOCl/RGO/PCN catalyst performs the best activity, showing the highest conversion rate of 71.6% along with a ca. 99% high selectivity to benzaldehyde. Blank experiment in the absence of visible light was also performed, and negligible conversion of benzyl alcohol is observed therefore confirming the requisite of visible-light illumination in the reaction. It can be found that BiOCl catalyst shows no reaction activity, which is resulted from its nonresponsivity to visible light. For the performance of CN, PCN and BiOCl/PCN samples, the conversion rate order is the same as the trend of photodegradation of TC, which is BiOCl/PCN > PCN > CN, indicating that the conversion rate of benzyl alcohol increased with the protonation of pristine g-C_3N_4 and further improved with the coupling of BiOCl.

Photocatalytic mechanism

Figure 9 displays the Z-scheme charge transfer in BiOCl/RGO/PCN photocatalyst. In view of that the optical adsorption edge of PCN exhibited a little redshift compared to pristine CN in above UV–Vis DRS spectra, the band edge positions of PCN would be different from that of pristine CN. The band edge positions of PCN in this study are estimated according to the following formulas [64]:

$$E_{VB} = \chi - E_e + 0.5E_g$$

$$E_{CB} = E_{VB} - E_g$$

where E_e represents the energy of free electrons of the hydrogen (~ 4.50 eV) and χ represents the absolute electronegativity of the semiconductor (4.82 eV for carbon nitride semiconductor) [65]. The CB and VB of PCN are calculated to be − 1.02 eV and + 1.67 eV by the band gap of 2.69 eV. Under simulated solar light irradiation, both BiOCl and PCN are excited to generate electron–hole pairs and the electrons simultaneously transferred from VBs to CBs. If the charge transfer directions between different semiconductors follow the double charge transfer theory (path I), the photoinduced electrons in the CB of PCN would migrate to the CB of BiOCl through RGO since the E_{CB} value of PCN (− 1.02 eV) is more negative than that of BiOCl (+ 0.1 eV) [22], while the photoinduced holes would transfer from the VB of BiOCl

Table 2 Photocatalytic oxidation of benzyl alcohol over different catalysts

Entry	Catalyst	Light	Time (h)	Conversion (%)	Selectivity (%)
1	CN	+	10	19.2	> 99
2	PCN	+	10	30.4	> 99
3	BiOCl	+	10	0	/
4	BiOCl/PCN	+	10	55.2	> 99
5	BiOCl/RGO/PCN	+	10	71.6	> 99
6	BiOCl/RGO/PCN	−	10	0.1	/

The reaction conditions: benzyl alcohol (0.5 mmol), CH_3CN solvent (10 mL), catalyst (50 mg), O_2 bubbling, room temperature, visible-light irradiation time = 10 h

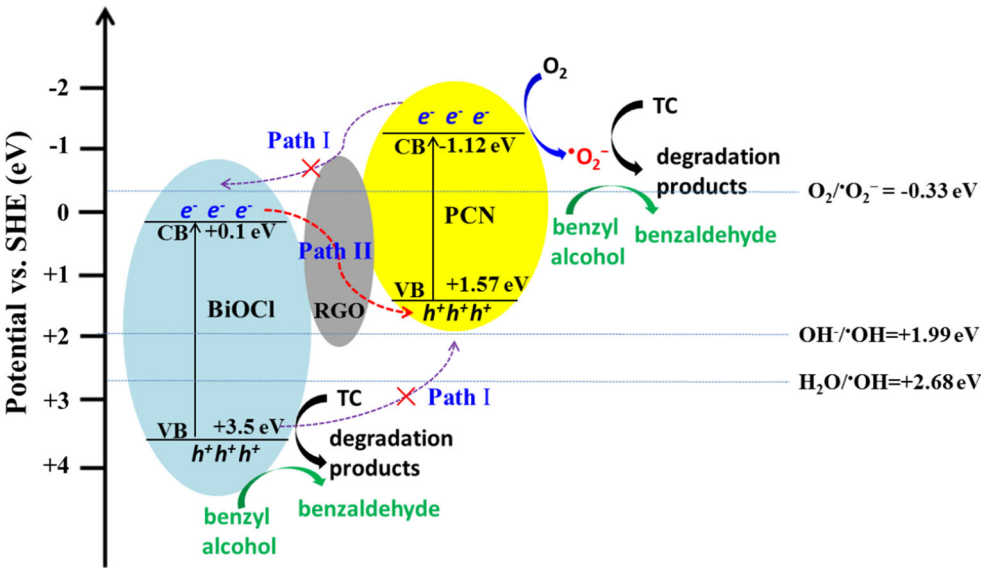

Figure 9 Schematic diagram for photoinduced charge carrier separation and transportation in BiOCl/RGO/PCN photocatalyst under simulated solar light irradiation.

(E_{VB}= 3.5 eV) [22] to the VB of PCN (E_{VB}=-+ 1.67 eV). Since the standard redox potential of $O_2/{}^{\cdot}O_2^-$ (− 0.33 eV) [66] is more negative than E_{VB} of BiOCl, electrons aggregated in the CB of BiOCl cannot reduce O_2 to form ${}^{\cdot}O_2^-$. However, we verified that ${}^{\cdot}O_2^-$ is the major reactive species over BiOCl/RGO/PCN photocatalyst in the above radical trapping experiments, which means the generation of ${}^{\cdot}O_2^-$ in the reaction is conclusive. If we regard BiOCl/RGO/PCN composite as a Z-scheme photocatalytic system (path II), when BiOCl, RGO and PCN are closely joined together, the electrons in the CB of BiOCl would transfer to the VB of PCN through the excellent electron transporting material RGO and recombine with the photoinduced holes on the VB of PCN. Therefore, more electrons and holes could stay in the CB of PCN and VB of BiOCl without the decrease in reduction and oxidation abilities, respectively. Since the E_{VB} value of PCN is more negative than the standard redox potential of $O_2/{}^{\cdot}O_2^-$, the electrons that stayed in the CB of PCN can react with O_2 to produce ${}^{\cdot}O_2^-$. Meanwhile, in view of the above control experiment (Fig. 8b) pointed out that the ${}^{\cdot}OH$ radicals were barely involved in the reaction, and the holes left in the VB of BiOCl are supposed to directly interact with the reaction substrates instead of reacting with H_2O or OH^- to generate ${}^{\cdot}OH$. In this respect, the Z-scheme mechanism is more reasonable than double charge transfer mechanism in BiOCl/RGO/PCN photocatalyst, and BiOCl/RGO/PCN Z-scheme photocatalytic system can facilitate the effective separation of photogenerated electrons and holes, as well as reserve the excellent redox ability of charge carriers.

Conclusions

In summary, a ternary BiOCl/RGO/PCN Z-scheme photocatalyst with closely contacted interface was successfully fabricated. The as-prepared BiOCl/RGO/PCN exhibited significantly enhanced photocatalytic activities

toward antibiotic TC degradation and selective oxidation of benzyl alcohol compared to pristine g-C_3N_4, protonated g-C_3N_4, pure BiOCl and binary BiOCl/PCN composite under simulated solar light irradiation. The confirmed Z-scheme photocatalytic system could result in more photoinduced electrons and holes retained in the CB of PCN and in the VB of BiOCl with the reserved excellent redox ability, respectively, which is greatly conducive to the further effective generation of active radicals participating in photocatalytic reaction. The research results revealed that the main factors affecting the photocatalytic activities include the spatially effective separation of photogenerated charge pairs, the fast transfer of electrons as well as the light harvesting ability. This work provides a way for promoting the construction of Z-scheme ternary photocatalyst with RGO as an electron transfer mediator via a facile synthetic method, as well as promoting its potential application in environmental purification and oxidative organic transformation.

Acknowledgements

This work was supported by the National Natural Science Foundation of China (Grant Nos. 21808019, 41641032, 41772240, 21407079 and 91544220), the Major Research Development Program of Jiangsu Province (BY2016030-15), the Science and Technology Bureau of Changzhou (CJ20179037), Science and Technology Project of Changzhou University (ZMF17020042), and the Science Foundation of Jiangsu University of Technology (KYY17001).

Compliance with ethical standards

Conflict of interest The authors declare that they have no conflict of interests.

References

[1] Singh R, Dutta S (2018) A review on H_2 production through photocatalytic reactions using TiO_2/TiO_2-assisted catalysts. Fuel 220:607–620

[2] Li H, Li J, Ai ZH, Jia FL, Zhang LZ (2018) Oxygen vacancy-mediated photocatalysis of BiOCl: reactivity, selectivity, and perspectives. Angew Chem Int Edit 57(1):122–138

[3] Mamba G, Mishra AK (2016) Graphitic carbon nitride (g-C_3N_4) nanocomposites: a new and exciting generation of visible light driven photocatalysts for environmental pollution remediation. Appl Catal B-Environ 198:347–377

[4] Natarajan TS, Thampi KR, Tayade RJ (2018) Visible light driven redox-mediator-free dual semiconductor photocatalytic systems for pollutant degradation and the ambiguity in applying Z-scheme concept. Appl Catal B-Environ 227:296–311

[5] Liu HJ, Du CW, Bai HK, Su YZ, Wei DD, Wang YQ, Liu GG, Yang L (2018) Fabrication of plate-on-plate Z-scheme SnS_2/Bi_2MoO_6 heterojunction photocatalysts with enhanced photocatalytic activity. J Mater Sci 53(15):10743–10757. https://doi.org/10.1007/s10853-018-2296-2

[6] Shi YN, Chen JJ, Mao ZY, Fahlman BD, Wang DJ (2017) Construction of Z-scheme heterostructure with enhanced photocatalytic H_2 evolution for g-C_3N_4 nanosheets via loading porous silicon. J Catal 356:22–31

[7] Jiang ZF, Wan WM, Li HM, Yuan SQ, Zhao HJ, Wong PK (2018) A hierarchical Z-scheme alpha-Fe_2O_3/g-C_3N_4 hybrid for enhanced photocatalytic CO_2 reduction. Adv Mater 30(10):1706108

[8] You ZY, Shen QH, Su YX, Yu Y, Wang H, Qin T, Zhang F, Cheng D, Yang H (2018) Construction of a Z-scheme core-shell g-C_3N_4/MCNTs/BiOI nanocomposite semiconductor with enhanced visible-light photocatalytic activity. New J Chem 42(1):489–496

[9] Wen JQ, Xie J, Chen XB, Li X (2017) A review on g-C_3N_4-based photocatalysts. Appl Surf Sci 391:72–123

[10] Li HY, Gan SY, Wang HY, Han DX, Niu L (2015) Intercorrelated superhybrid of AgBr supported on graphitic-C_3N_4-decorated nitrogen-doped graphene: high engineering photocatalytic activities for water purification and CO_2 reduction. Adv Mater 27(43):6906–6913

[11] Wang XC, Maeda K, Thomas A, Takanabe K, Xin G, Carlsson JM, Domen K, Antonietti M (2009) A metal-free polymeric photocatalyst for hydrogen production from water under visible light. Nat Mater 8(1):76–80

[12] Ding F, Yang D, Tong ZW, Nan YH, Wang YJ, Zou XY, Jiang ZY (2017) Graphitic carbon nitride-based nanocomposites as visible-light driven photocatalysts for environmental purification. Environ Sci-Nano 4(7):1455–1469

[13] Suyana P, Ganguly P, Nair BN, Mohamed AP, Warrier KGK, Hareesh US (2017) Co_3O_4–C_3N_4 p–n nano-heterojunctions for the simultaneous degradation of a mixture of pollutants under solar irradiation. Environ Sci-Nano 4(1):212–221

[14] Zhang SW, Gao HH, Liu X, Huang YS, Xu XJ, Alharbi NS, Hayat T, Li JX (2016) Hybrid 0D–2D nanoheterostructures: in situ growth of amorphous silver silicates dots on g-C_3N_4 nanosheets for full-spectrum photocatalysis. ACS Appl Mater Interfaces 8(51):35138–35149

[15] Fageria P, Uppala S, Nazir R, Gangopadhyay S, Chang CH, Basu M, Pande S (2016) Synthesis of monometallic (Au and

Pd) and bimetallic (AuPd) nanoparticles using carbon nitride (C_3N_4) quantum dots via the photochemical route for nitrophenol reduction. Langmuir 32(39):10054–10064

[16] Sun M, Zeng Q, Zhao X, Shao Y, Ji PG, Wang CQ, Yan T, Du B (2017) Fabrication of novel g-C_3N_4 nanocrystals decorated Ag_3PO_4 hybrids: enhanced charge separation and excellent visible-light driven photocatalytic activity. J Hazard Mater 339:9–21

[17] Zhou L, Zhang W, Chen L, Deng HP (2017) Z-scheme mechanism of photogenerated carriers for hybrid photocatalyst Ag_3PO_4/g-C_3N_4 in degradation of sulfamethoxazole. J Colloid Interfaces Sci 487:410–417

[18] Tan YG, Shu Z, Zhou J, Li TT, Wang WB, Zhao ZL (2018) One-step synthesis of nanostructured g-C_3N_4/TiO_2 composite for highly enhanced visible-light photocatalytic H_2 evolution. Appl Catal B-Environ 230:260–268

[19] Wang JC, Yao HC, Fan ZY, Zhang L, Wang JS, Zang SQ, Li ZJ (2016) Indirect Z-Scheme BiOl/g-C_3N_4 photocatalysts with enhanced photoreduction CO_2 activity under visible light irradiation. ACS Appl Mater Interfaces 8(6):3765–3775

[20] Ma S, Xie J, Wen JQ, He KL, Li X, Liu W, Zhang XC (2017) Constructing 2D layered hybrid CdS nanosheets/MoS_2 heterojunctions for enhanced visible-light photocatalytic H_2 generation. Appl Surf Sci 391:580–591

[21] Zhu MY, Liu Q, Chen W, Yin YY, Ge L, Li HN, Wane K (2017) Boosting the visible-light photoactivity of BiOCl/$BiVO_4$/N-GQD ternary heterojunctions based on internal Z-scheme charge transfer of N-GQDs: simultaneous band gap narrowing and carrier lifetime prolonging. ACS Appl Mater Interfaces 9(44):38832–38841

[22] Bai Y, Wang PQ, Liu JY, Liu XJ (2014) Enhanced photocatalytic performance of direct Z-scheme BiOCl–g-C_3N_4 photocatalysts. RSC Adv 4(37):19456–19461

[23] Bai Y, Chen T, Wang PQ, Wang L, Ye LQ, Shi X, Bai W (2016) Size-dependent role of gold in g-C_3N_4/BiOBr/Au system for photocatalytic CO_2 reduction and dye degradation. Sol Energ Mater Sol C 157:406–414

[24] Wu JJ, Shen XP, Miao XL, Ji ZY, Wang JH, Wang T, Liu MM (2017) An all-solid-state Z-Scheme g-C_3N_4/Ag/Ag_3VO_4 photocatalyst with enhanced visible-light photocatalytic performance. Eur J Inorg Chem 21:2845–2853

[25] Ma D, Wu J, Gao MC, Xin YJ, Chai C (2017) Enhanced debromination and degradation of 2,4-dibromophenol by an Z-scheme Bi_2MoO_6/CNTs/g-C_3N_4 visible light photocatalyst. Chem Eng J 316:461–470

[26] Che HN, Liu CB, Hu W, Hu H, Li JQ, Dou JY, Shi WD, Li CM, Dong HJ (2018) NGQD active sites as effective collectors of charge carriers for improving the photocatalytic performance of Z-scheme g-C_3N_4/Bi_2WO_6 heterojunctions. Catal Sci Technol 8(2):622–631

[27] Brigante M, Schulz PC (2011) Remotion of the antibiotic tetracycline by titania and titania-silica composed materials. J Hazard Mater 192(3):1597–1608

[28] Xue JJ, Ma SS, Zhou YM, Zhang ZW, He M (2015) Facile photochemical synthesis of Au/Pt/g-C_3N_4 with plasmon-enhanced photocatalytic activity for antibiotic degradation. ACS Appl Mater Interfaces 7(18):9630–9637

[29] Mboula VM, Hequet V, Gru Y, Colin R, Andres Y (2012) Assessment of the efficiency of photocatalysis on tetracycline biodegradation. J Hazard Mater 209:355–364

[30] Xie ZJ, Feng YP, Wang FL, Chen DN, Zhang QX, Zeng YQ, Lv WY, Liu GG (2018) Construction of carbon dots modified MoO_3/g-C_3N_4 Z-scheme photocatalyst with enhanced visible-light photocatalytic activity for the degradation of tetracycline. Appl Catal B-Environ 229:96–104

[31] Luo BF, Chen M, Zhang ZY, Xu J, Li D, Xu DB, Shi WD (2017) Highly efficient visible-light-driven photocatalytic degradation of tetracycline by a Z-scheme g-C_3N_4/Bi_3TaO_7 nanocomposite photocatalyst. Dalton Trans 46(26):8431–8438

[32] Guo F, Shi WL, Wang HB, Han MM, Li H, Huang H, Liu Y, Kang ZH (2017) Facile fabrication of a CoO/g-C_3N_4 p–n heterojunction with enhanced photocatalytic activity and stability for tetracycline degradation under visible light. Catal Sci Technol 7(15):3325–3331

[33] Zhang YH, Tang ZR, Fu X, Xu YJ (2011) Engineering the unique 2D mat of graphene to achieve graphene-TiO_2 nanocomposite for photocatalytic selective transformation: what advantage does graphene have over its forebear carbon nanotube? ACS Nano 5(9):7426–7435

[34] Qin N, Liu YH, Wu WM, Shen LJ, Chen X, Li ZH, Wu L (2015) One-Dimensional CdS/TiO_2 nanofiber composites as efficient visible-light-driven photocatalysts for selective organic transformation: synthesis, characterization, and performance. Langmuir 31(3):1203–1209. https://doi.org/10.1021/la503731y

[35] Wang Y, Wang XC, Antonietti M (2012) Polymeric graphitic carbon nitride as a heterogeneous organocatalyst: from photochemistry to multipurpose catalysis to sustainable chemistry. Angew Chem Int Ed 51(1):68–89

[36] Wang ZT, Song YJ, Zou JH, Li LY, Yu Y, Wu L (2018) The cooperation effect in the Au–Pd/LDH for promoting photocatalytic selective oxidation of benzyl alcohol. Catal Sci Technol 8(1):268–275

[37] Zhang LG, Liu D, Guan J, Chen XF, Guo XC, Zhao FH, Hou TG, Mu XD (2014) Metal-free g-C_3N_4 photocatalyst by sulfuric acid activation for selective aerobic oxidation of benzyl alcohol under visible light. Mater Res Bull 59:84–92

[38] Verma S, Baig RBN, Nadagouda MN, Varma RS (2016) Selective oxidation of alcohols using photoactive VO@g-C_3N_4. ACS Sustain Chem Eng 4(3):1094–1098

[39] Yuan MQ, Tian F, Li GF, Zhao HP, Liu YL, Chen R (2017) Fe(III)-modified BiOBr hierarchitectures for improved photocatalytic benzyl alcohol oxidation and organic pollutants degradation. Ind Eng Chem Res 56(20):5935–5943

[40] Ramacharyulu PVRK, Abbas SJ, Sahoo SR, Ke SC (2018) Mechanistic insights into 4-nitrophenol degradation and benzyl alcohol oxidation pathways over MgO/g-C_3N_4 model catalyst systems. Catal Sci Technol 8(11):2825–2834

[41] Shen J, Xue JJ, He GY, Ni J, Chen ZX, Tang B, Zhou ZW, Chen HQ (2018) Construction of 3D marigold-like Bi_2WO_6/Ag_2O/CQDs heterostructure with superior visible-light active photocatalytic activity toward tetracycline degradation and selective oxidation. J Mater Sci 53(17):12040–12055. https://doi.org/10.1007/s10853-018-2479-x

[42] Hummers WS, Offeman RE (1958) Preparation of graphitic oxide. J Am Chem Soc 80(6):1339

[43] Meng SG, Ye XJ, Ning XF, Xie ML, Fu XL, Chen SF (2016) Selective oxidation of aromatic alcohols to aromatic aldehydes by BN/metal sulfide with enhanced photocatalytic activity. Appl Catal B-Environ 182:356–368

[44] Liu Y, Yan K, Zhang JD (2016) Graphitic carbon nitridesensitized with CdS quantum dots for visible-light-driven photoelectrochemical aptasensing of tetracycline. ACS Appl Mater Interfaces 8(42):28255–28264

[45] Liu WW, Shang YY, Zhu AQ, Tan PF, Liu Y, Qiao LL, Chu DW, Xiong X, Pan J (2017) Enhanced performance of doped BiOCl nanoplates for photocatalysis: understanding from doping insight into improved spatial carrier separation. J Mater Chem A 5(24):12542–12549

[46] Bao YC, Chen KZ (2018) Novel Z-scheme BiOBr/reduced graphene oxide/protonated g-C_3N_4 photocatalyst: synthesis, characterization, visible light photocatalytic activity and mechanism. Appl Surf Sci 437:51–61

[47] Ong WJ, Tan LL, Chai SP, Yong ST, Mohamed AR (2015) Surface charge modification via protonation of graphitic carbon nitride (g-C_3N_4) for electrostatic self-assembly construction of 2D/2D reduced graphene oxide (rGO)/g-C_3N_4 nanostructures toward enhanced photocatalytic reduction of carbon dioxide to methane. Nano Energy 13:757–770

[48] Zhao QH, Xing YX, Liu ZL, Ouyang J, Du CF (2018) Synthesis and characterization of modified BiOCl and their application in adsorption of low-concentration dyes from aqueous solution. Nanoscale Res Lett 13:69

[49] Gao FD, Zeng DW, Huang QW, Tian SQ, Xie CS (2012) Chemically bonded graphene/BiOCl nanocomposites as high-performance photocatalysts. Phys Chem Chem Phys 14(30):10572–10578

[50] Xia PF, Zhu BC, Cheng B, Yu JG, Xu JS (2018) 2D/2D g-C_3N_4/MnO_2 nanocomposite as a direct Z-Scheme photocatalyst for enhanced photocatalytic activity. ACS Sustain Chem Eng 6(1):965–973

[51] Ding J, Xu W, Wan H, Yuan DS, Chen C, Wang L, Guan GF, Dai WL (2018) Nitrogen vacancy engineered graphitic C_3N_4-based polymers for photocatalytic oxidation of aromatic alcohols to aldehydes. Appl Catal B-Environ 221:626–634

[52] Ye LQ, Tian LH, Peng TY, Zan L (2011) Synthesis of highly symmetrical BiOI single-crystal nanosheets and their 001 facet-dependent photoactivity. J Mater Chem 21(33): 12479–12484

[53] Wang XJ, Wang Q, Li FT, Yang WY, Zhao Y, Hao YJ, Liu SJ (2013) Novel BiOCl-C_3N_4 heterojunction photocatalysts: in situ preparation via an ionic-liquid-assisted solvent-thermal route and their visible-light photocatalytic activities. Chem Eng J 234:361–371

[54] Kruk M, Asefa T, Coombs N, Jaroniec M, Ozin GA (2002) Synthesis and characterization of ordered mesoporous silicas with high loadings of methyl groups. J Mater Chem 12(12):3452–3457

[55] Li X, Yu JG, Jaroniec M (2016) Hierarchical photocatalysts. Chem Soc Rev 45(9):2603–2636

[56] Zhang YW, Liu JH, Wu G, Chen W (2012) Porous graphitic carbon nitride synthesized via direct polymerization of urea for efficient sunlight-driven photocatalytic hydrogen production. Nanoscale 4(17):5300–5303

[57] Hu SZ, Zhang WD, Bai J, Lu G, Zhang L, Wu G (2016) Construction of a 2D/2D g-C_3N_4/rGO hybrid heterojunction catalyst with outstanding charge separation ability and nitrogen photofixation performance via a surface protonation process. RSC Adv 6(31):25695–25702

[58] Martha S, Nashim A, Parida KM (2013) Facile synthesis of highly active g-C_3N_4 for efficient hydrogen production under visible light. J Mater Chem A 1(26):7816–7824

[59] Feng X, Zhang WD, Deng H, Ni ZL, Dong F, Zhang YX (2017) Efficient visible light photocatalytic NOx removal with cationic Ag clusters-grafted $(BiO)_2CO_3$ hierarchical superstructures. J Hazard Mater 322:223–232

[60] Bellardita M, Garcia-Lopez EI, Marci G, Krivtsov I, Garcia JR, Palmisano L (2018) Selective photocatalytic oxidation of aromatic alcohols in water by using P-doped g-C_3N_4. Appl Catal B-Environ 220:222–233

[61] Su FZ, Mathew SC, Lipner G, Fu XZ, Antonietti M, Blechert S, Wang XC (2010) mpg-C_3N_4-catalyzed selective oxidation of alcohols Using O_2 and visible light. J Am Chem Soc 132(46):16299–16301

[62] Lima MJ, Tavares PB, Silva AMT, Silva CG, Faria JL (2017) Selective photocatalytic oxidation of benzyl alcohol

to benzaldehyde by using metal-loaded g-C_3N_4 photocatalysts. Catal Today 287:70–77

[63] Liu Y, Zhang P, Tian BZ, Zhang JL (2015) Core-shell structural CdS@SnO_2 nanorods with excellent visible-light photocatalytic activity for the selective oxidation of benzyl alcohol to benzaldehyde. ACS Appl Mater Interfaces 7(25):13849–13858

[64] Li XZ, Yan XY, Lu XW, Zuo SX, Li ZY, Yao C, Ni CY (2018) Photo-assisted selective catalytic reduction of NO by Z-scheme natural clay based photocatalyst: insight into the effect of graphene coupling. J Catal 357:59–68

[65] Han Q, Wang B, Gao J, Cheng ZH, Zhao Y, Zhang ZP, Qu LT (2016) Atomically thin mesoporous nanomesh of graphitic C_3N_4 for high-efficiency photocatalytic hydrogen evolution. ACS Nano 10(2):2745–2751

[66] Xu DF, Cheng B, Cao SW, Yu JG (2015) Enhanced photocatalytic activity and stability of Z-scheme Ag_2CrO_4-GO composite photocatalysts for organic pollutant degradation. Appl Catal B-Environ 164:380–388